City Research Online

City, University of London Institutional Repository

This is the accepted version of the paper.

This version of the publication may differ from the final published version.

Real-time battery temperature monitoring using FBG sensors: a data-driven calibration method

Li Zhang, Xuan Liu, Kang Li, Dajun Du, Min Zheng, Qun Niu, Yi Yang, Qi Zhou, Tong Sun, and Kenneth TV Grattan

Abstract— Battery storage has an important role to play in integrating large scale renewable power generations and in transport decarbonization. Real-time monitoring of battery temperature profile is indispensable for battery safety management. Due to the advantages of small size, resistance to corrosion, immunity to electromagnetic interference, and multiplexing, fiber Bragg-grating (FBG) sensing has received substantial interests in recent years for battery temperature measurement. However, traditional temperature calibration for FBG sensors often requires a high-standard reference, and cause the sensors fail to be consistent during the calibration or re-calibration processes. To tackle the challenges, an ensemble data-driven calibration method is developed in this paper for FBG sensors. The calibration model consists of a linear part and a nonlinear part. First, the fuzzy C-means (FCM) algorithm is used to extract the linear relationship between the measured FBG wavelength shift and temperature variation. Then, the empirical mode decomposition (EMD) technique is used to classify the intrinsic mode functions (IMFs) and the remainder for the unmodeled nonlinear information. The unmodeled nonlinear information is further compensated using battery state of charge (SOC) and cycle number information. The experimental results confirm that the proposed temperature calibration method achieves desirable accuracy and reliability, with both the mean absolute error and root mean square error being around 0.2 ℃ respectively. Compared with the traditional temperature calibration method, the proposed approach can be used online in real-life applications.
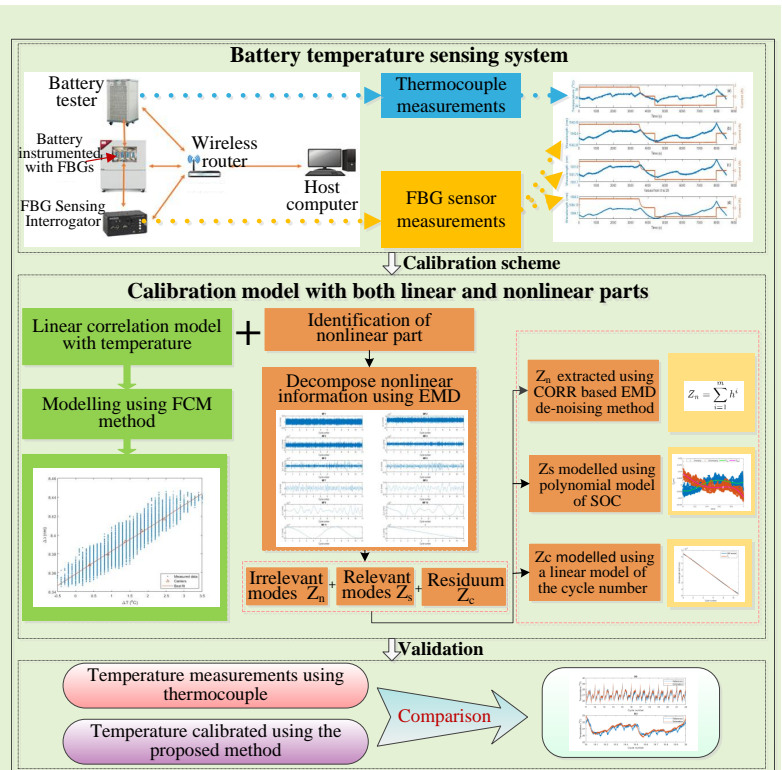
Index Terms— Lithium-ion battery, Data-driven method, Temperature calibration, FBG, EMD

Li Zhang, Dajun Du, Min Zheng and Qun Niu are with Shanghai Key Laboratory of Power Station Automation Technology, School of Mechatronic Engineering and Automation, Shanghai University, Shanghai 200072, China (e-mail: zl_qee@163.com, ddj@i.shu.edu.cn, zhengmin203@shu.edu.cn, nq@shu.edu.cn).

Li Zhang, Xuan Liu and Kang Li are with School of Electronic and Electrical Engineering, University of Leeds, Leeds, LS2 9JT, UK (e-mail: zl_qee@163.com, elxl@leeds.ac.uk, k.li1@leeds.ac.uk).

Yi Yang and Qi Zhou are with State Grid Jiangsu Electric Power Research Institute, 211103 Nanjing, China (e-mail: yang_yi_ee@163.com, dianqizhouqi@163.com).

Tong Sun and Kenneth TV Grattan are with School of Mechatronics, Computer Science and Engineering, City university of London, London, EC1V 0HB, UK (e-mail:t.sun@city.ac.uk, k.t.v.grattan@city.ac.uk).

I. INTRODUCTION

LITHIUM-ION batteries have several distinctive advantages such as high energy density and high power density, which have been increasingly used in power grids [1]–[3] and in electric vehicles (EVs) [4]–[6]. Temperature seriously influences the performance of a lithium-ion battery such as the usable capacity and internal resistance. It has been widely recognized that inappropriate operation temperature can accelerate the degradation of lithium-ion batteries [7], [8]. Furthermore, during the charging/discharging process, heat is accumulating. In particular, under abuse conditions such as overcharging, it may cause overtemperature and even explosion. Therefore, to guarantee the operational safety, thermal management plays an essential role in the battery management system

(BMS).

Thermocouple and thermistor have been the most popular temperature sensors for battery temperature monitoring [9]. However, they are sensitive to corrosion and electromagnetic radiation and each temperature measuring point needs a separate data channel. For an energy storage system (ESS), this will significantly increase the number of sensors and other supporting facilities, which makes the already limited space even more compacted, particularly in EVs. Therefore, the Fiber Bragg-grating (FBG) sensors are attracting increasing interests in battery management due to the advantages of smaller size, mechanical robustness, resistance to corrosion and immune to electromagnetic interference [10], [11]. Moreover, a single optical fiber can be inscribed with multiple FBG sensors for temperature measurements, which can save a lot of cost and space [12]. In general, the FBG sensors can be attached to specific locations on the battery shell to monitor the surface temperature [13], or insert inside the battery to measure its internal temperature [14]. Thereinto, the encapsulation cells should be fabricated from scratch by manufacturers, otherwise it will damage the cells or change their performances to insert the FBG sensors into the commercial cells [15]. While the temperature sensors have been successfully bonded on the surface of commercial cells [12], [16], and the surface mount FBG sensors can be easily scaled up to battery packs where accurately monitoring the temperature profile of cells inside the packs are extremely important for safe operation of the packages. Thus, in this study, the surface mounting FBGs will be applied to commercial cells to improve measurement accuracy.

In summary, FBG sensors have been chosen as one of the most suitable means to allow practical measurements to be taken due to advanced packing technologies [17] and the inherent advantages that they have for a range of applications such as civil structure applications [17] and the battery temperature monitoring and estimation under investigation in this paper. The specific benefits of fiber optical sensors have been discussed by some of the authors in detail in other publications [18] but they are particularly well suited to these situations where electrical monitoring is unsafe in harsh environment, thereby offering a significant safety advantage. Further, fiber optical sensing methods such as are used here work well when electrical means of monitoring fail, for example where there is a large amount of electromagnetic noise, and data being read from conventional sensors can be corrupted. In addition, when there are a large number of sensors to be placed such as battery temperature profile monitoring in this paper, the FBG sensors are easy to install and lightweight. Finally, the use of FBG networks can offer a competitive costing option, especially when safety is to the fore in the measurement.

FBG sensors measure temperature which induces change in the effective refractive index of the core and the grating period, thus resulting in a shift of the reflected spectrum [19]. Meanwhile, any external strain will also contribute to a peak shift in the reflected wavelength. The resonant wavelength peak shift is generally created by the variations of both temperature and strain. To decouple the impacts of the temperature from the strain, various methods have been proposed [20]–[22], however temperature calibration is a prerequisite for all these methods.

Generally speaking, temperature calibration needs to be conducted in a controlled environment. For example, constant specific external temperature environments controlled by a thermal chamber should be applied. The external temperature should be kept for a long enough period to ensure the temperature homogeneity in both the battery specimen and FBG sensor. The thermo-optic coefficient and the host material thermal expansion coefficient can be calibrated consequently [20]. Although this temperature calibration method can accurately identify the relevant parameters, some issues still exist. Firstly, the calibration method can only be performed offline and the whole process is extremely demanding and time consuming. Secondly, the method requires a high-precision thermal chamber to ensure the reliability of the calibration results, therefore it is not suitable for online real-time applications.

To overcome the shortcomings of the traditional temperature calibration method for FBG sensors, a novel data-driven calibration method is developed in this paper. The main contributions are summarized as follows:

- FBG sensors are applied to commercial 18650 LiFePO4 lithium-ion battery cells for multi-point temperature measurements. Since the wavelength shift are the results of temperature variation, strain change and other unknown factors, both the state of charge (SOC) and the aging are taken into account to estimate the temperature.
- A novel temperature calibration model is developed which comprises a linear part and a nonlinear compensation part, where Fuzzy C-means algorithm is used to establish the linear relationship between the measured wavelength shift and temperature variation, and the remaining wavelength information is decomposed into the intrinsic mode functions (IMFs) and the residuum using the empirical mode decomposition (EMD) method. Then the irrelevant modes are selected from IMFs to represent the effect by the measurement noise, while the relevant modes are selected from the IMFs represents the effect of the SOC and the residuum is used to represent the aging effect.
- To build nonlinear compensation part of the temperature calibration model, the relevant modes relating to SOC is represented using a polynomial model, while the residuum relating to the cycle number is modeled using a linear function.
- Experimental results confirm that the proposed approach is capable of producing accurate and comparable temperature estimations as the conventional temperature sensors without resorting to expensive

and laborious offline laboratory calibrations.

The remainder of this paper is organized as follows. The experimental setup is briefly introduced in Section II. The framework of the data-drive calibration method is detailed in Section III. Experimental study is presented in Section IV to verify efficacy of the developed method, and a conclusion is made in Section V.

II. EXPERIMENTAL SETUP

Four commercial 18650 LiFePO$_4$ lithium-ion battery cells (#1, #2, #3, #4) are used, which have a nominal voltage of 3.2 V and capacity of 1.6 Ah. FBG sensors are mounted on the surfaces of the battery cells. In this study, each cell uses three FBG sensors, namely FBG 1, FBG 2 and FBG 3, as shown in Fig. 1.
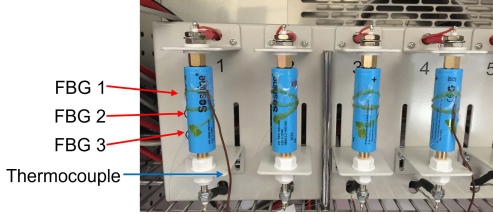

Fig. 1: The layout of the FBG sensors

The FBG sensors are interfaced with a Micron-Optics interrogator for measurements, and a thermocouple is also attached to the location close to the FBG sensors as a reference. Typically, the resolution and the accuracy tolerance of the FBG sensors are 1 pm and ±0.5 nm respectively, while for the thermocouples, these are 0.1 ℃ and ±1 ℃ respectively. The battery experiments are managed by a NEWARE battery test system to cycle the cells under the room temperature environment and the current and voltage signals are collected. The experimental set-up is shown in Fig. 2.
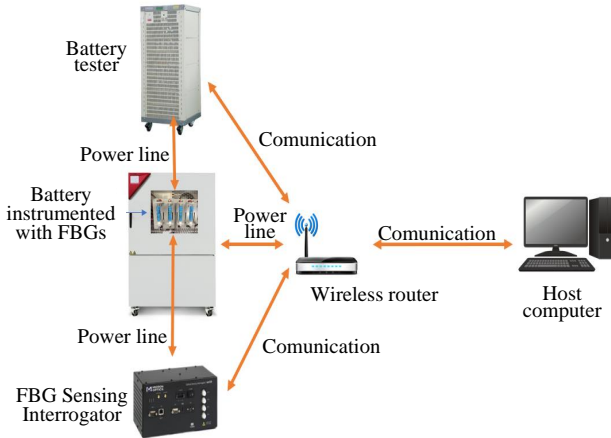

Fig. 2: Battery test system

In this study, a standard Constant-Current Constant-Voltage (CC-CV) charging process and a Constant-Current (CC) discharging process are applied to the test

cell, where the cell is first charged with constant a 1.6 A current until the terminal voltage reaches the upper cutoff voltage (3.6 V). Then the cell is charged under the constant voltage mode until the charging current decreases to 75 mA. The sampling frequency for all the measurement equipment is set at 1 Hz. For the CC discharging process, a 1.6 A constant current is used to discharge the cell to the lower cutoff voltage of 2.0 V. The resting time between the charging and consequent discharging phase is set to 10 minutes. The characteristic wavelengths of FBGs 1, 2 and 3 are 1534 nm, 1539 nm and 1544 nm, respectively. The measurements of cell #1 are shown in Fig. 3.
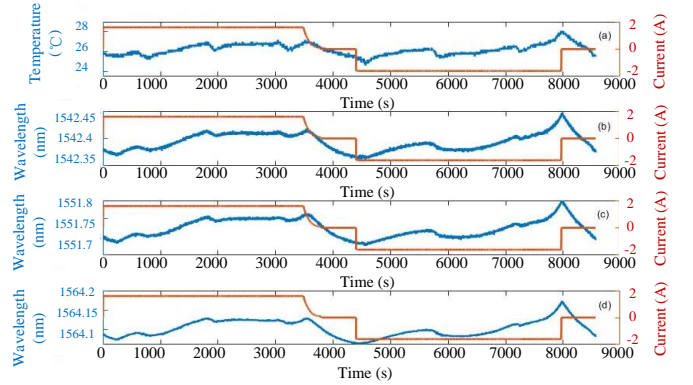

Fig. 3: The temperature and peak wavelengths measured during the charging and discharging process

III. THE PROPOSED DATA-DRIVEN CALIBRATION METHOD

In this section, the temperature measurements by FBG sensors are calibrated via a linear model combined with a nonlinear compensation model. The linear correlation model is built using the fuzzy C-means algorithm, while the nonlinear compensation model is built using the EMD method. The data-driven calibration methodology is elaborated below.

A. Problem formulation

Generally speaking, a FBG sensor will reflect a certain narrow band of spectrum and the centered peak wavelength is known as the Bragg wavelength [23], [24] which will shift due to several factors, such as thermal and mechanical effects, and this can be expressed as:

$$\lambda_B = 2n_e\Lambda \tag{1}$$

where n_e is the effective refractive index at the grating location and Λ is the grating period [20]. The wavelength shift ($\Delta\lambda_B$) due to temperature variation (ΔT) and strain variation ($\Delta\varepsilon$) can be expressed as follows:

$$\frac{\Delta\lambda_B}{\lambda_B} = (\alpha + \xi)\Delta T + (1 - P_e)\Delta\varepsilon \tag{2}$$

where P_e is the photo-elastic coefficient, α is the thermal expansion coefficient and ξ is the thermo-optic coefficient

[24] of the fiber material. Both temperature variation ΔT and strain change ($\Delta\varepsilon$) are unknown, hence to estimate the temperature variation, Eq. (2) can be simplified as follows:

$$\Delta\lambda_B = f(\Delta T) + Z \qquad (3)$$

where $f(\Delta T) = \lambda_B(\alpha + \xi)\Delta T$ is the effect of temperature variation on the wavelength shift, while Z represents the remainder wavelength shift.

It is worth noting that in this paper, wavelength shift is expressed as a combination of thermal output and mechanical strain in Eq. (2), where the first term represents the lumped thermal effect including the thermo-optic effect and thermal apparent strain, and the second term represent the lumped mechanical strain effect. For the first term, the main contributor is the variation of the silica refraction index, induced by the thermo-optic effect, while the effect induced by thermal expansion which alters the period of the microstructure, is marginal. Since the wavelength shift due to temperature variation is modelled as a linear function as elaborated earlier, hence errors induced by the linear model is lumped into the second term Z in Eq. (3), which will be modeled using a nonlinear function elaborated below.

It is clear that Z represents the lumped contribution of the strain variation and other captured factors or modeling errors on $\Delta\lambda_B$. Hence,

$$\Delta T = (\Delta\lambda_B - Z)/(\alpha + \xi) = f^{-1}(\Delta\lambda_B - Z) \qquad (4)$$

It is also worth noting that both the thermal expansion coeicient and the thermo-optic coeicient vary with the temperature, hence the FBG wavelength response to the temperature is a nonlinear relationship in general. However, these coeicients are often treated as constants if the temperature does not change significantly or in cases where very high precision requirement on temperature measurement is not required [25]. In other words, $f(\cdot)$ is usually treated as a linear function over the room temperature range, while the higher order nonlinear relationships are ignored. In an experimental study on temperature measurement using FBG sensors at 1550 nm [26], a nonlinear temperature response model was built where the quadratic term in the Bragg wavelength shift is approaching to a constant from 0 °C to 40 °C at 1549 nm. Therefore, in this paper the wavelength shift to the temperature variation is treated as a linear relationship, while the impact of Z on the wavelength shift is represented by a nonlinear function.

In this paper, the base temperature (T_0) is set at 25 °C, the temperature estimated via the FBG sensor, namely T_{FBG} can be expressed as

$$T_{FBG} = T_0 + \Delta T = T_0 + f^{-1}(\Delta\lambda_B - Z) \qquad (5)$$

where $\Delta\lambda_B = \lambda - \lambda_0$. λ and λ_0 represent the measured peak wavelength and the characteristic wavelength of the FBG sensor. Note that this temperature estimation

equation is generic and suitable for different batteries and FBG sensors made of different materials. Here, the temperature model includes both a linear part f and a nonlinear part Z which can be constructed below.

B. Fuzzy C-means method to identify the linear model

The relationship between temperature variation and wavelength shift was investigated in [16], [22], [27], and their relationship is a linear function. A detailed investigation of FBG 1 attached on cell #1 is given below. The measured cell surface temperature variation ΔT and the measured wavelength shift $\Delta\lambda_B$ are shown in Fig. 4. It is clear that the temperature responses of the FBG wavelength is approximately linear.
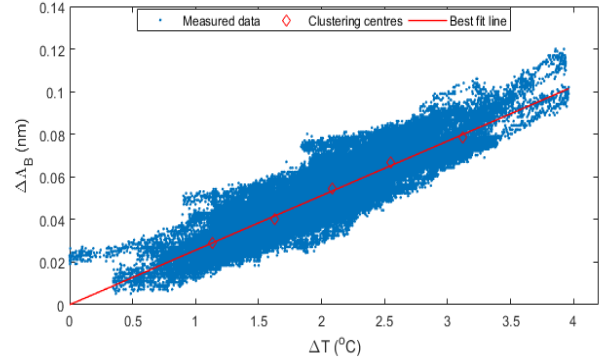

Fig. 4: Relationship between ΔT and $\Delta\lambda_B$ via FBG 1 of cell #1

In order to extract the temperature effect, clustering methods are used to extract the relationship between the temperature variation ΔT and the wavelength shift $\Delta\lambda_B$. Among the various clustering methods, Fuzzy C-means (FCM) is a popular clustering method due to its robustness to ambiguities and it can extract much more information than hard clustering methods [28]. FCM is an iterative process which partitions the input data into a certain number of clusters with the respect to the membership value and the distance. The objective function of FCM can be expressed as

$$J_m(U, P) = \sum_{j=1}^{N} \sum_{i=1}^{c} (\mu_{ij})^m (d_{ij})^2 \qquad (6)$$

where N is the number of input data, P is the cluster center matrix, U is the membership function matrix. μ_{ij} is the likelihood value which presents the degree of the ith input data belonging to the jth cluster, which satisfies the constraints in Eq. (7). m is the fuzziness parameter which is used to set the fuzziness of the cluster. d_{ij} is the distance between the ith input data and the jth cluster center. In this paper, the distance refers to the Euclidean distance.

$$\begin{cases} \sum_{i=1}^{c} \mu_{ij} = 1, j = 1, 2, ..., N \\ 0 \leq \mu_{ij} \leq 1, i = 1, 2, ..., c, j = 1, 2, ..., N \\ 0 < \sum_{j=1}^{N} \mu_{ij} < N, i = 1, 2, ..., c \end{cases} \quad (7)$$

By applying the Lagrangian multiplier technique, the membership function can be calculated as follows:

$$\mu_{ij}^{t} = \frac{1}{\sum_{k=1}^{c} \left(\frac{d_{ij}}{d_{kj}}\right)^{\frac{2}{m-1}}} \quad (8)$$

where t is the number of iterations. The new cluster center can be calculated as

$$P_{i}^{(t+1)} = \frac{\sum_{j=1}^{N} (\mu_{ij}^{(t)})^m x_j}{\sum_{j=1}^{N} (\mu_{ij}^{(t)})^m} \quad (9)$$

The center of each cluster is considered to be the representative sample of the measurements in each cluster. Therefore, the relationship between the temperature variation and wavelength shift can be extracted in term of the relationship between the cluster centres. Various number of clustering centres are tested in this study, the results show that the minimum residual can be obtained when the number of cluster centres is 5. For the case of FBG 1 on cell #1 as shown in Fig. 4, the clustering centres obtained by the FCM are presented as the red circles in Fig. 4, and the solid line shows the best fit. For each cluster center, its projection on the y-axis represents the wavelength shift $\Delta\lambda_B$ caused by the corresponding temperature variation ΔT on the x-axis. Then the linear fitting process using the clustering centres is repeated 10 times to obtain the average parameters. Thus, the linear relationship between ΔT and $\Delta\lambda_B$ is expressed as

$$f(\Delta T) = 0.0255\Delta T + 8.358 \quad (10)$$

Obviously, Eq. (10) is equivalent to the first term in Eq. (2). Thus, the slope of this linear fitting equation can be regarded as the thermal sensitivity of the FBGs, which is considered as 25.5 pm/°C. Our previous work [11] has indicated that the sensitivity to temperature of such the surface mounted FBG sensor is on average 21 pm/°C. This is because the optical fiber will be stretched during installation and the cured glue will change the thermal conductivity. It is clear that the proposed method is viable and the remainder of the wavelength shifts can also be viewed as the result of the strain effect.

C. EMD method to construct the nonlinear model

The linear model considers the impact of temperature on the wavelength shift ($\Delta\lambda_B$). However, $\Delta\lambda_B$ is also affected by the mechanical strain, uncaptured thermal effect from the linear model, and some unknown factors, which can be lumped as the model residual (Z). Generally speaking, the strain variation represents the dimensional

change of the cell. Due to the coupling of temperature and strain, the strain is obviously caused by thermal expansion, which is reflected in the electrode expansion and hence electrode volume change. In addition to temperature effects which is already modeled using the linear function elaborated above, the strain variation of a lithium-ion battery is caused by the following factors, such as the electrode expansion and contraction with lithium intercalation/deintercalation, electrode volume change with the irreversible reaction deposits, and the dead volume and pressure change depending on the cell construction [29].

In this study, the cell structure is fixed, only the reversible electrode expansion and contraction and irreversible electrode volume change are analysed. Hence, Z can be modelled by using the combination of the short time effect and the long time effect. The short time effect considers the electrode change in each cycle due to the intercalation/deintercalation of lithium ions, which is also affected by the temperature [30]. Furthermore, the change of SOC due to the strain variation of the electrodes of the lithium-ion batteries has been researched [23], [30]–[32]. Thus, SOC is selected as the main contributor to the short-term strain variation.

In regard to the long time effect, the intercalation/deintercalation of lithium ions, which is increased or decreased in speed by the temperature. It induced mechanical stress to the graphite lattice, which causes the crack and expansion of the electrode [33]. The electrode induces the irreversible volume change because of the cycle aging, leading to the strain change of cell shell. The experimental results [31] also indicated that the maximum strain of the electrode decreases with the increasing of the cycle number.

In summary, to compensate the temperature model, Z is modeled as a function of both the SOC and cycle numbers which will be elaborated in the following.

1) Decomposition of Z using EMD: Since Z is obtained by extracting $f(\Delta T)$ from $\Delta\lambda_B$, the measurement noise of ΔT from the thermocouple and the measurement noise of $\Delta\lambda_B$ from the FBG sensor are introduced. Therefore, Z will be decomposed into three groups, denoted as Z_n, Z_s and Z_c and $Z = Z_n + Z_s + Z_c$, where Z_n represents the measurement noise, Z_s represents the effect of the change of cell SOC, and Z_c represents the effect of battery aging hence is a function of the cycle number respectively. Empirical mode decomposition (EMD) technique is used in this study to decompose Z. EMD is an adaptive time-space analysis method proposed by Huang et al. [34] for non-stationary and non-linear signals. EMD break down any signal Z into a number of L components called intrinsic mode functions (IMFs) without leaving the time domain. The accumulation of the extracted IMFs with the residual can restore the decomposed signal, thus, Z can be expressed as

$$Z = \sum_{i=1}^{L} h^i + r \quad (11)$$

where h^i represents the ith IMF and r is the residual of the decomposition.

The flow chart of EMD algorithm is shown in Fig.5. Accordingly, the implementation steps of the EMD algorithm can be summarized as follows.
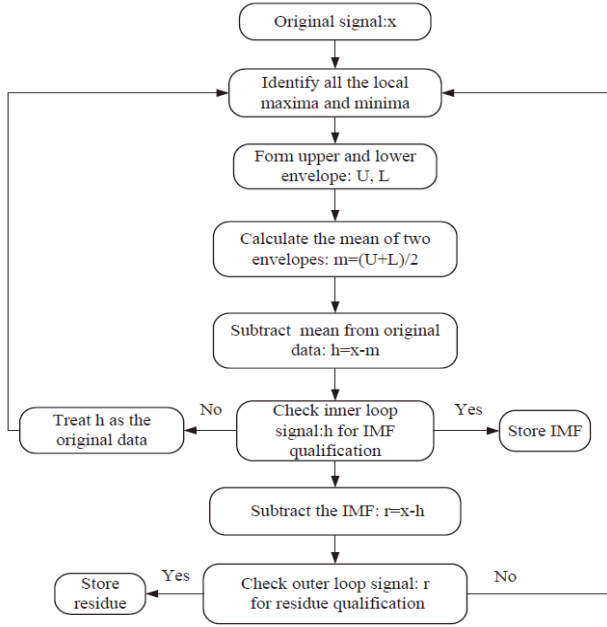

Fig. 5: The flow chart of EMD algorithm

Step 1 Initialisation: Set $i = 1$, $n = 1$, $r_0 = Z$.

Step 2 Set $k = 1$, $h_{i,0} = r_{k-1}$.

Step 3 Identify all local maxima and minima of $h_{i,k-1}$.

Step 4 Construct the upper envelope, namely $U_{i,k-1}$ and the lower envelope, namely $L_{i,k-1}$ via the cubic splines interpolation.

Step 5 Determine the mean, namely $m_{i,k-1}$ of $U_{i,k-1}$ and $L_{i,k-1}$. $m_{i,k-1} = \frac{1}{2}(U_{i,k-1} - L_{i,k-1})$.

Step 6 Calculate the ith IMF after k^{th} iteration: $h_{i,k} = h_{i,k-1} - m_{i,k-1}$.

1. if $h_{i,k}$ does not satisfies the IMF criteria, increase k as $k = k+1$ and repeat Step 3 to 6.

2. if $h_{i,k}$ satisfies the IMF criteria, then set $h_i = h_{i,k}$ and $r_i = r_{i-1} - h_i$.

Step 7 If r_i represents a residuum, set $r = r_i$ and stop the process. If not, increase i as $i = i + 1$ and repeat Step 2 to 6.

For the remainder of Z, the extracted IMFs are illustrated in Fig.6.

Among the decomposed modes, the irrelevant modes can be used to represent Z_n and the relevant modes can be used to represent Z_s and the residuum can be used to represent Z_c. The three modes are modelled using different methods as follows.

2) Modelling Z_n: The correlation coefficient (CORR) based EMD de-noising method [35] is applied to select the irrelevant modes in this study for the calculation of Z_n. Defines m as the indicator when the correlation coefficient between Z and $Z - Z_n$ starts to decrease sharply, Z_n is thus can be expressed as

$$Z_n = \sum_{i=1}^{m} h^i \qquad (12)$$

Then the data of FBG 1 on cell #1 is trained for 10 times under same conditions. The correlation coefficients between Z and $Z - Z_n$ obtained with various values of m is presented in Fig. 7. It is evident that once m is greater than 5, the correlation coefficient between Z and $Z - Z_n$ decreases significantly every time. Therefore, m is set to 5 for FBG 1 on cell #1.

3) Modelling Z_s: To capture the relationship between cell SOC and Z_s, coulomb counting method is applied to calculate the SOC value of the cell in both charging and discharging processes. The distribution of Z_s on each point SOC is presented in Fig. 8. There is a clear difference between the distributions of Z_s in the charging and discharging processes. Polynomial fitting technique is then applied to fit the relationships between the cell SOC and Z_s in the charging and discharging processes, named Z_{ch} and Z_{dis} respectively. Therefore, Z_s can be expressed as

$$Z_s(t) = \begin{cases} Z_{ch}(t), & I \geq 0 \\ Z_{dis}(t), & I < 0 \end{cases} \qquad (13)$$

where I represents the current through the cell at time t. $Z_{ch}(t)$ and $Z_{dis}(t)$ can be expressed as

$$\begin{cases} Z_{ch}(t) = p_1 s^4 + p_2 s^3 + p_3 s^2 + p_4 s + p_5 \\ Z_{dis}(t) = q_1 s^4 + q_2 s^3 + q_3 s^2 + q_4 s + q_5 \end{cases} \qquad (14)$$

where s represents the SOC value of the cell at time t, p_1 to p_5, and q_1 to q_5 are the fitting coefficients of Z_{ch} and Z_{dis} respectively. The fitting coefficients can be identified by using the least squares (LS) method. The identification results of FBG 1 on cell #1 which are the average value of 10 times repeated training are given in Table I.

4) Modelling Z_c: As elaborated earlier, Z_c is used to describe the relationship between Z and the cell cycle number c. The average distribution of the EMD residual r is shown in Fig. 9, it is clear that r presents an almost linear downward trend with the increasing of cycle number. Therefore, Z_c of FBG 1 on cell #1 can be expressed as follows:

$$Z_c = -0.0014c + 0.009 \qquad (15)$$

In summary, Z_s and Z_c can be obtained according to Eq. (13) to (15). The system compensation Z can be calculated as the sum of Z_s and Z_c. Thus, according to Eq. (5), the estimation of temperature (T_{FBG}) can be calculated as follows

$$T_{FBG} = T_0 + f^{-1}((\lambda - \lambda_0) - (Z_s + Z_c)) \qquad (16)$$

where λ and λ_0 represent the measured peak wavelength and the characteristic wavelength of the FBG sensor. The identification of Z_s and Z_c is essential for different FBGs or different cells with different materials.
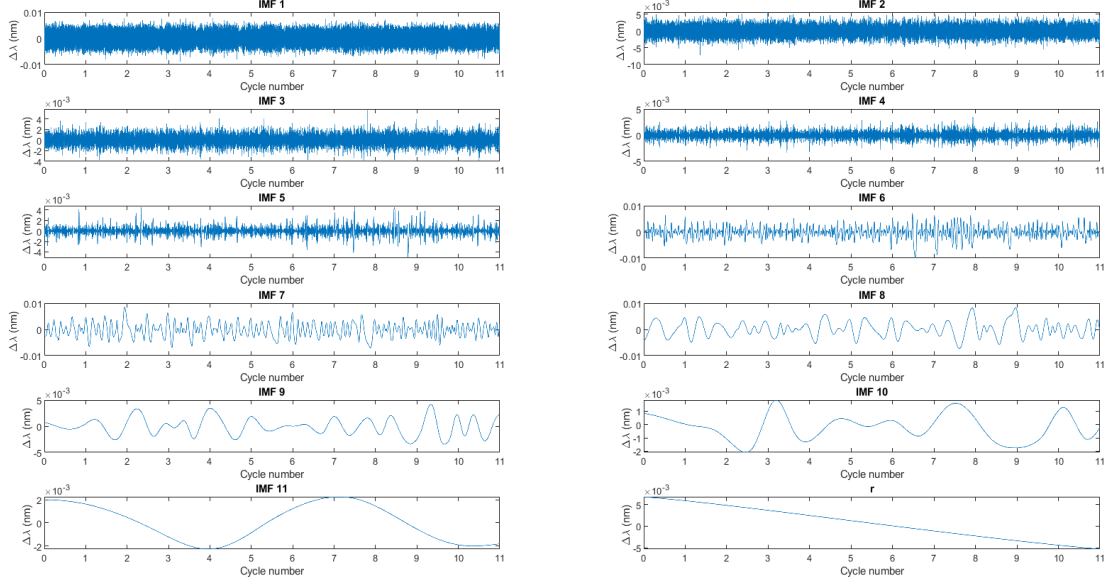
Fig. 6: The decomposed modes and residual via FBG 1 of cell #1

TABLE I: The identified fitting coefficients for Z_{ch} and Z_{dis}

Coefficient	p_1	p_2	p_3	p_4	p_5	q_1	q_2	q_3	q_4	q_5
Value	0.0554	-0.1784	0.1501	-0.0294	-0.0009	-0.0893	0.1205	-0.0134	-0.0352	0.0103
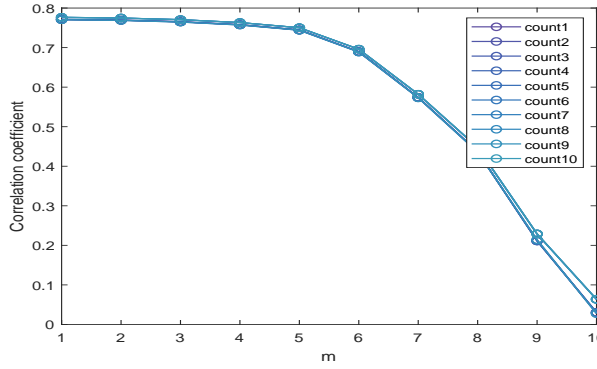
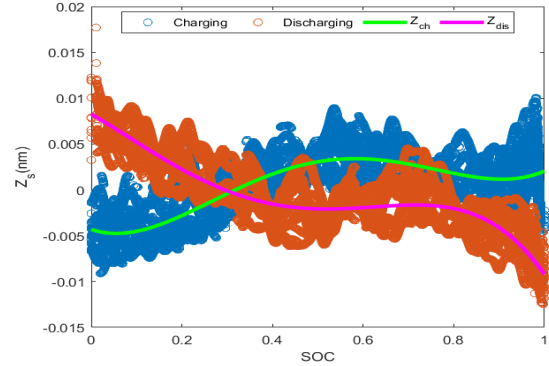Fig. 7: Correlation with m repeating 10 times via FBG 1 of cell #1

Fig. 8: The distribution of Z_s on SOC via FBG 1 of cell #1

IV. EXPERIMENTAL RESULTS AND DISCUSSIONS

In order to verify the accuracy and reliability of the proposed temperature calibration method, the data from the first 11 cycles of cell #1 are used for training, while the data of another 13 cycles (the 12th to the 24th cycle) of cell #1 is used for the validation. The reference temperature value is measured by the thermocouple. Coulomb counting method is used to calculate the SOC of the cell.

The temperature estimated via FBG 1 using the above proposed method is shown in Fig. 10. It is evident that the temperature estimated by the proposed method matches well with the reference temperature measured

by the thermocouple. The validation of a cycle using the developed method is shown in Fig. 11. It is clear that most of the errors are distributed within ± 0.5 °C, only except for the points at high and low SOC levels where the errors are almost ± 1 °C, which is still acceptable for the thermocouple accuracy tolerance level. Furthermore, the 1 °C error at high or low SOC levels has negligible impacts on fault diagnose [36] which often uses much larger temperature differences in setting the fault thresholds. From Fig. 11, the variation of the estimated temperature is found to be similar to the variation of the reference temperature which is often used to estimate SOC or
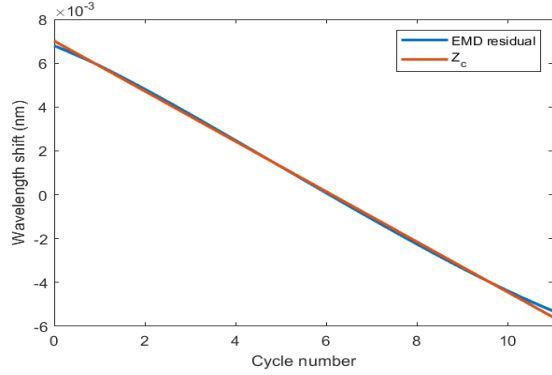
Fig. 9: The distribution of EMD residual verses cycle number via FBG 1 of cell #1
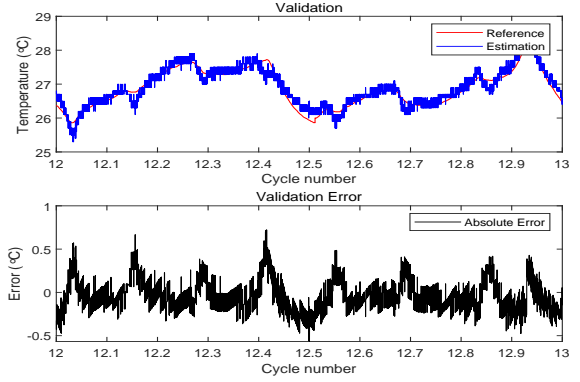

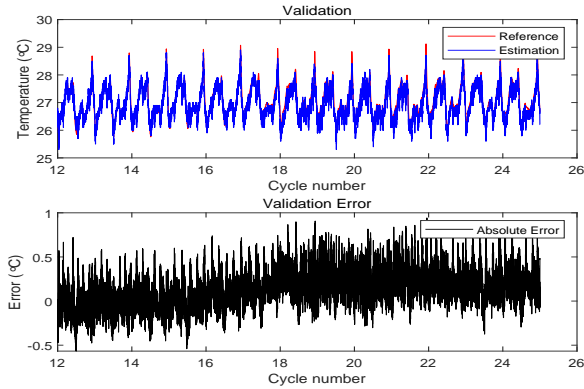Fig. 11: Validation results of Cycle #12 via FBG 1 of cell #1

capacity [37].

Fig. 10: Temperature validation via FBG 1 of cell #1

Fig. 12: Temperature validation via FBG 2 of cell #1

Then the proposed method is applied to the signals obtained from other FBGs attached on cell #1, and the temperature estimation results via FBGs 2 and 3 are also analyzed. Similarly, the data collected in Cycles 1 to 11 is used for modelling and the data obtained in Cycles 12 to 24 is used for validation. The temperature validation results of FBGs 2 and 3 are shown in Figs. 12-15, respectively. It can be seen that the temperature estimations obtained via FBGs 1, 2 and 3 are highly consistent with the temperature data measured via the thermocouple.

Furthermore, the root mean square error (RMSE), mean absolute error (MAE), maximum absolute error (MaxAE), mean error (ME) and variance (Var) of the validation results are listed in Table II.

TABLE II: The statistics of the estimated temperature of cell #1

	RMSE	MAE	MaxAE	ME	Var
FBG1	0.2	0.2	1	0.1	0.04
FBG2	0.3	0.2	1	0.1	0.05
FBG3	0.2	0.2	0.9	0.1	0.04
Avg	0.2	0.2	1	0.1	0.04

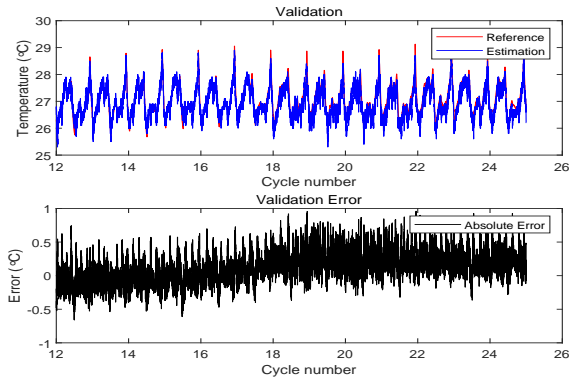The statistics of the estimation errors also indicates that the proposed method can accurately estimate the battery shell temperature via the peak wavelength data obtained using different FBG sensors. This again confirms the validity and effectiveness of the proposed method.

To further verify the effectiveness of the proposed method, FBG 1 of cell #4 is calibrated for the surface temperature. The data from the first 11 cycles of cell #4 are used for training, while the data from the 15th to the 27th cycle of cell #4 is used for validation. The validation results are illustrated in Figs. 16 and 17 and the statistics of the estimated errors are given in Table III.

TABLE III: The statistics of estimated temperature of cell #4

	RMSE	MAE	MaxAE	ME	Var
FBG1	0.2	0.2	1.2	0.1	0.1

It is clear that the proposed calibration method once again achieves better estimation results on cell #4 which are validated on different cycles. It again confirms the effectiveness of the proposed method.

V. CONCLUSIONS

This paper has presented a novel data-driven based FBG sensor temperature calibration method that can perform FBG temperature calibration online, which will
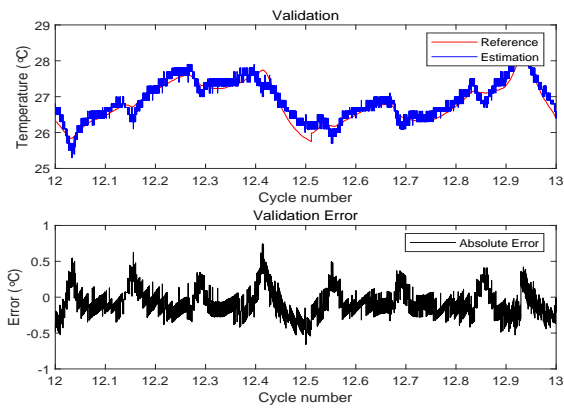
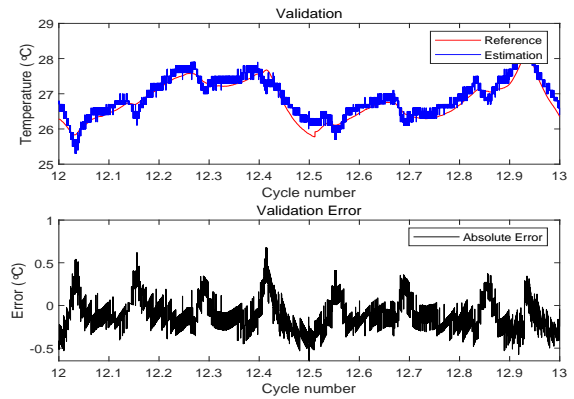Fig. 13: Validation results of cycle #12 via FBG 2 of cell #1

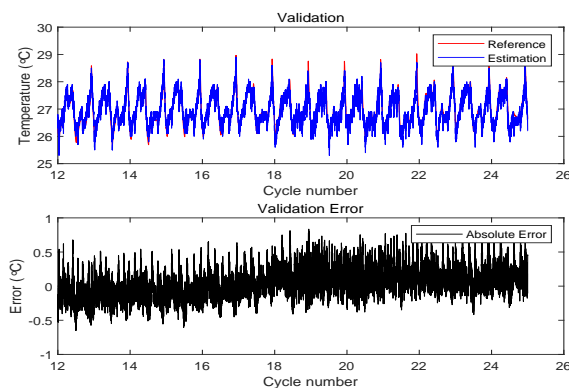Fig. 15: Validation results of cycle #12 via FBG 3 of cell #1

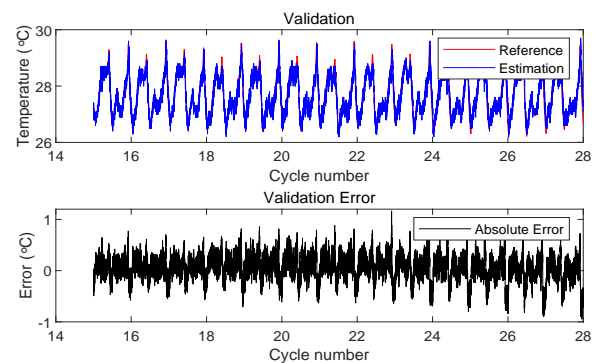Fig. 14: Temperature validation via FBG 3 of cell #1

Fig. 16: Temperature validation via FBG 1 of cell #4

not interrupt the normal operation of the ESSs. The proposed method does not require high-standard laboratory equipment and environment, which makes it more friendly to use in real life applications. In the experiments, it is shown that the proposed temperature calibration method has achieved desirable estimation accuracy and reliability, with both the mean absolute error and root mean square error being 0.2 ℃. Due to the unstable electrochemical reactions inside the cell at high and low SOC levels, the strain variations of the cell become more difficult to capture by Z_s, resulting in slightly large errors within ± 1 ℃ which will be still acceptable for the sate estimation and fault diagnoses in BMS, which will be further validated in our future work. In the study, the proposed method has been applied to different FBG sensors and different battery cells, and it will also be extended to other batteries made of different materials in the future work.

REFERENCES

[1] D.-I. Stroe, V. Knap, M. Swierczynski, A.-I. Stroe, and R. Teodorescu, "Operation of a grid-connected lithium-ion battery energy storage system for primary frequency regulation: A battery lifetime perspective," IEEE Transactions on Industry Applications, vol. 53, no. 1, pp. 430–438, 2017.

[2] B. Xu, A. Oudalov, A. Ulbig, G. Andersson, and D. S. Kirschen, "Modeling of lithium-ion battery degradation for cell life assessment," IEEE Transactions on Smart Grid, vol. 9, no. 2, pp. 1131–1140, 2018.

[3] Y. Jin, Z. Zhao, S. Miao, Q. Wang, L. Sun, and H. Lu, "Explosion hazards study of grid-scale lithium-ion battery energy storage station," Journal of Energy Storage, vol. 42, p. 102987, 2021.

[4] K. Liu, L. I. Kang, P. Qiao, and Z. Cheng, "A brief review on key technologies in the battery management system of electric vehicles," Frontiers of Mechanical Engineering, vol. 14, no. 1, p. 47–64, 2019.

[5] C. Zhang, K. Li, S. Mcloone, and Z. Yang, "Battery modelling methods for electric vehicles - a review," in 2014 European Control Conference (ECC), 2014, pp. 2673–2678.

[6] C. Zhang, K. Li, J. Deng, and S. Song, "Improved realtime state-of-charge estimation of lifepo $_4$ battery based on a novel thermoelectric model," IEEE Transactions on Industrial Electronics, vol. 64, no. 1, pp. 654–663, 2017.

[7] M. Petzl, M. Kasper, and M. A. Danzer, "Lithium plating in a commercial lithium-ion battery–a low-temperature aging study," Journal of Power Sources, vol. 275, pp. 799–807, 2015.

[8] X. Feng, M. Ouyang, X. Liu, L. Lu, Y. Xia, and X. He, "Thermal runaway mechanism of lithium ion battery for electric vehicles: A review," Energy Storage Materials, vol. 10, pp. 246–267, 2018.

[9] L. Raijmakers, D. Danilov, R.-A. Eichel, and P. Notten, "A review on various temperature-indication methods for li-ion batteries," Applied energy, vol. 240, pp. 918–945, 2019.

[10] S. Novais, M. Nascimento, L. Grande, M. F. Domingues, P. Antunes, N. Alberto, C. Leitão, R. Oliveira, S. Koch, G. T. Kim et al., "Internal and external temperature monitoring of a li-ion battery with fiber bragg grating sensors," Sensors, vol. 16, no. 9, p. 1394, 2016.

[11] B. Rente, M. Fabian, M. Vidakovic, X. Liu, X. Li, K. Li, T. Sun, and K. T. V. Grattan, "Lithium-ion battery state-of-charge estimator based on fbg-based strain sensor and employing machine learning," IEEE Sensors Journal, vol. 21, no. 2, pp.
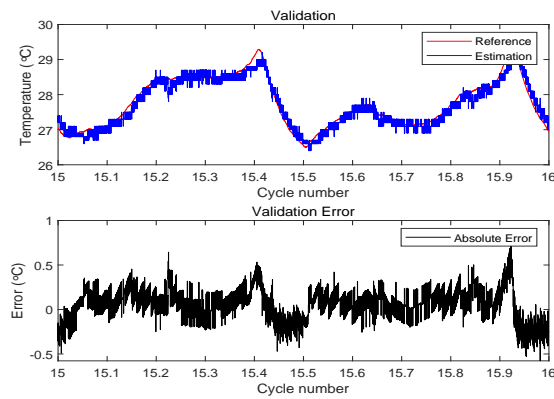
Fig. 17: Validation results of cycle #15 via FBG 1 of cell #4

1453–1460, 2021.

[12] J. Peng, S. Jia, H. Yu, X. Kang, S. Yang, and S. Xu, "Design and experiment of fbg sensors for temperature monitoring on external electrode of lithium-ion batteries," IEEE Sensors Journal, vol. 21, no. 4, pp. 4628–4634, 2021.

[13] S. Panchal, I. Dincer, M. Agelin-Chaab, R. Fraser, and M. Fowler, "Experimental and theoretical investigation of temperature distributions in a prismatic lithium-ion battery," International Journal of Thermal Sciences, vol. 99, pp. 204–212, 2016.

[14] C. Zhang, K. Li, and J. Deng, "Real-time estimation of battery internal temperature based on a simplified thermoelectric model," Journal of Power Sources, vol. 302, pp. 146–154, 2016.

[15] E. McTurk, T. Amietszajew, J. Fleming, and R. Bhagat, "Thermo-electrochemical instrumentation of cylindrical li-ion cells," Journal of Power Sources, vol. 379, pp. 309–316, 2018.

[16] Nascimento, Micael and Ferreira, Marta S and Pinto, João L, "Temperature fiber sensing of li-ion batteries under different environmental and operating conditions," Applied Thermal Engineering, vol. 149, pp. 1236–1243, 2019.

[17] Y. B. Lin, K. C. Chang, J. C. Chern, and L. A. Wang, "Packaging methods of fiber-bragg grating sensors in civil structure applications," IEEE Sensors Journal, vol. 5, pp. 419–424, 2005.

[18] K. T. V. Grattan and B. T. E. Meggitt, Optical Fiber Sensor Technology. London, UK: Chapman & Hall, 1995.

[19] Y. Zhao and Y. Liao, "Discrimination methods and demodulation techniques for fiber bragg grating sensors," Optics and Lasers in Engineering, vol. 41, no. 1, pp. 1–18, 2004.

[20] G. Pereira, M. McGugan, and L. P. Mikkelsen, "Method for independent strain and temperature measurement in polymeric tensile test specimen using embedded fbg sensors," Polymer Testing, vol. 50, pp. 125–134, 2016.

[21] Z. Kang, J. Sun, Y. Bai, and S. Jian, "Twin-core fiber-based erbium-doped fiber laser sensor for decoupling measurement of temperature and strain," IEEE Sensors Journal, vol. 15, no. 12, pp. 6828–6832, 2015.

[22] G. Yang, C. Leitão, Y. Li, J. Pinto, and X. Jiang, "Real-time temperature measurement with fiber bragg sensors in lithium batteries for safety usage," Measurement, vol. 46, no. 9, pp. 3166–3172, 2013.

[23] J. Peng, X. Zhou, S. Jia, Y. Jin, S. Xu, and J. Chen, "High precision strain monitoring for lithium ion batteries based on fiber bragg grating sensors," Journal of Power Sources, vol. 433, p. 226692, 2019.

[24] C. Hong, C. Bao, J. Fei, Y. Zhang, and X. Wang, "Application of fbg technology in additive manufacturing: Monitoring real-time internal temperature of products," IEEE Sensors Journal, vol. 21, no. 5, pp. 6003–6011, 2021.

[25] J. Zhang and Y. Li, "Calibration method for fiber bragg grating temperature sensor," in 2009 9th International Conference on Electronic Measurement & Instruments, 2009, pp. 2–822–2–825.

[26] G. Flockhart, R. Maier, J. S. Barton, W. N. Macpherson, J. Jones, K. E. Chisholm, Z. Lin, I. Bennion, I. Read, and P. D. Foote, "Quadratic behavior of fiber bragg grating temperature

coefficients," Applied Optics, vol. 43, no. 13, pp. 2744–2751, 2004.

[27] M. Nascimento, M. S. Ferreira, and J. L. Pinto, "Real time thermal monitoring of lithium batteries with fiber sensors and thermocouples: A comparative study," Measurement, vol. 111, pp. 260–263, 2017.

[28] Y. Lu, T. Ma, C. Yin, X. Xie, W. Tian, and S. Zhong, "Implementation of the fuzzy c-means clustering algorithm in meteorological data," International Journal of Database Theory and Application, vol. 6, no. 6, pp. 1–18, 2013.

[29] J. H. Lee, H. M. Lee, and S. Ahn, "Battery dimensional changes occurring during charge/discharge cycles—thin rectangular lithium ion and polymer cells," Journal of power sources, vol. 119, pp. 833–837, 2003.

[30] L. W. Sommer, P. Kiesel, A. Ganguli, A. Lochbaum, B. Saha, J. Schwartz, C.-J. Bae, M. Alamgir, and A. Raghavan, "Fast and slow ion diffusion processes in lithium ion pouch cells during cycling observed with fiber optic strain sensors," Journal of Power Sources, vol. 296, pp. 46–52, 2015.

[31] A. Ganguli, B. Saha, A. Raghavan, P. Kiesel, K. Arakaki, A. Schuh, J. Schwartz, A. Hegyi, L. W. Sommer, A. Lochbaum et al., "Embedded fiber-optic sensing for accurate internal monitoring of cell state in advanced battery management systems part 2: Internal cell signals and utility for state estimation," Journal of Power Sources, vol. 341, pp. 474–482, 2017.

[32] C.-J. Bae, A. Manandhar, P. Kiesel, and A. Raghavan, "Monitoring the strain evolution of lithium-ion battery electrodes using an optical fiber bragg grating sensor," Energy technology, vol. 4, no. 7, pp. 851–855, 2016.

[33] V. Agubra and J. Fergus, "Lithium ion battery anode aging mechanisms," Materials, vol. 6, no. 4, pp. 1310–1325, 2013.

[34] N. E. Huang, Z. Shen, S. R. Long, M. C. Wu, H. H. Shih, Q. Zheng, N.-C. Yen, C. C. Tung, and H. H. Liu, "The empirical mode decomposition and the hilbert spectrum for nonlinear and non-stationary time series analysis," Proceedings of the Royal Society of London. Series A: mathematical, physical and engineering sciences, vol. 454, no. 1971, pp. 903–995, 1998.

[35] Z. Shang-yue, L. Yuan-yuan, and Y. Gong-liu, "Emd interval thresholding denoising based on correlation coefficient to select relevant modes," in 2015 34th Chinese Control Conference (CCC). IEEE, 2015, pp. 4801–4806.

[36] J. Wei, G. Dong, and Z. Chen, "Lyapunov-based thermal fault diagnosis of cylindrical lithium-ion batteries," IEEE Transactions on Industrial Electronics, vol. 67, no. 6, pp. 4670–4679, 2020.

[37] A. El Mejdoubi, A. Oukaour, H. Chaoui, H. Gualous, J. Sabor, and Y. Slamani, "State-of-charge and state-of-health lithium-ion batteries' diagnosis according to surface temperature variation," IEEE Transactions on Industrial Electronics, vol. 63, no. 4, pp. 2391–2402, 2016.